IEEE Access
Multidisciplinary ⋮ Rapid Review ⋮ Open Access Journal

Received 29 July 2023, accepted 10 August 2023, date of publication 14 August 2023, date of current version 21 August 2023.

Digital Object Identifier 10.1109/ACCESS.2023.3305256

RESEARCH ARTICLE

A Multi-Spectral Image Database for In-Vivo Hand Perfusion Evaluation

OMAR GUTIERREZ-NAVARRO[1], (Member, IEEE), LILIANA GRANADOS-CASTRO[2], ALDO RODRIGO MEJIA-RODRIGUEZ[2], AND DANIEL U. CAMPOS-DELGADO[2,3], (Senior Member, IEEE)

[1]Departamento de Ingenieria Biomedica, Universidad Autonoma de Aguascalientes, Ags 20340, Mexico
[2]Facultad de Ciencias, Universidad Autonoma de San Luis Potosi, San Luis Potosi 78295, Mexico
[3]Instituto de Investigacion en Comunicacion Optica, Universidad Autonoma de San Luis Potosi, San Luis Potosi 78210, Mexico

Corresponding author: Omar Gutierrez-Navarro (omar.gutierrezn@edu.uaa.mx)

This work was supported in part by CONAHCYT: Consejo Nacional de Humanidades, Ciencias y Tecnologías under grant 321899, and the Universidad Autonoma de Aguascalientes under Grants PII22-2 and PII22-6N. The work of Liliana Granados-Castro was supported by CONACYT through a Doctoral Fellowship under Grant 881980.

This work involved human subjects or animals in its research. Approval of all ethical and experimental procedures and protocols was granted by the Comitê Institucional de Bioética de la Universidad Autonoma de Aguascalientes under Application No. CIB-UAA-37, and performed in line with the Declaration of Helsinki.

ABSTRACT The increasing prevalence of vascular diseases encourages the development of minimally invasive approaches to assess tissue perfusion. A significant challenge facing current state-of-the-art methods is their validation against clinical data. In this study, we introduce an open-source database designed to evaluate tissue perfusion during the application of an occlusion protocol. The database comprises sequences of multi-spectral images (visible and near-infrared region) from the subjects' predominant hand and their photoplethysmography data for validation. Our study recruited 45 healthy participants, including 21 females, with an age range between 18-24 years old (standard deviation equal to 1.73). The database was evaluated using two methods for estimating skin perfusion parameters based on multi-spectral images: a Kubelka-Munk model, and a linear regression. Meanwhile, for validation purposes, the changes in oxygenated and deoxygenated hemoglobin were evaluated by photoplethysmography data as baseline perfusion parameters. The Pearson correlation between plethysmography-based perfusion parameters and those extracted from multi-spectral images was evaluated in all cases as a validation metric. Our findings demonstrated a strong Pearson correlation ($\rho > 0.7$) between changes in oxygenated and deoxygenated hemoglobin and multi-spectral based perfusion parameters, suggesting that the database is useful for further research related to in-vivo perfusion assessment. The primary objective of this database is to provide open-source data from a controlled occlusion protocol to evaluate new approaches based on multi-spectral images in the visible and near-infrared regions. In addition, the validation by photoplethysmography data facilitates the development and assessment of innovative tissue perfusion estimation techniques.

INDEX TERMS Tissue perfusion monitoring, multi-spectral image processing, functional monitoring and imaging, tissue oxygenation, microcirculation.

I. INTRODUCTION

The human body runs on oxygen, nutrients and immune factors, which are transported by the circulatory and lymphatic systems, in a process known as tissular perfusion. Poor blood perfusion may cause problems such as ischemia, and additional complications may lead to organ damage or even failure. Impaired blood flow also affects wound healing [1], which can lead to infections in open wounds. In fact, this scenario is critical for diabetic patients, whose blood vessels in the lower extremities are usually affected by their condition [2].

The associate editor coordinating the review of this manuscript and approving it for publication was Zhen Ren.

At clinical level, physicians pay attention to variables that reflect the general state of perfusion throughout the body. It is common practice to evaluate temperature, skin color, and even perform some simple tests to assess capillary refill time by applying pressure to a fingernail [3]. Modern methods available may require the use of contrast agents, such as thermography, laser speckle contrast analysis [4], and indocyanine green fluorescent imaging [5]. In some cases, techniques such as magnetic resonance imaging [6], computer tomography [7], laser doppler imaging [8], multi-spectral optoacoustic tomography [9] and surface electrode approaches [10] can provide information about regional perfusion. There are perfusion tests available for specific organs, such as myocardial perfusion imaging, cerebral oximetry, renal scintigraphy, and hepatic vein characterization, just to name a few [11]. Nonetheless, there is a growing interest in the development of minimally invasive methods for perfusion estimation in large tissue regions. Such methods aim to characterize tissular perfusion at multiple positions up to the microcirculatory level [12]. Non-invasive imaging tests are generally safe, painless, and require minimal preparation. They serve as an initial screening tool and offer valuable information about organ function and health. However, they may have limitations in terms of resolution and sensitivity compared to invasive tests.

In this context, a common approach is to use imaging techniques, either reflectance or absorbance of light, from different portions of the spectra to measure a perfusion parameter. For instance, PulseCam [13] estimates maps of the pulsatile component (AC) of blood flow in the skin by using an RGB camera and reference photoplethysmography (PPG) values. The authors in [13] test their method by applying occlusion on healthy participants (vascular occlusion at 70 mmHg, and total occlusion at 140 mmHg) using a blood cuff on the arm. They evaluated a total of 12 participants with various skin tones (Fitzpatrick skin types I to V [14]).

Another approach using visible spectra is detailed in [15]. The proposed method estimates a video output corresponding to variations in finger blood perfusion on non-Euro-Americans subjects. Authors validate their approach by identifying ischemia in 10 volunteers, who underwent an occlusion test. This test lasted 10 min, 3 min without pressure, and 7 more with a tourniquet-induced occlusion.

Spectral imaging techniques capture radiation across multiple wavelengths, they are not restricted to the visible spectrum [16]. This includes infrared, multispectral, and hyperspectral modalities. These techniques can reveal properties not discernible with standard imaging approaches. As such, spectral imaging can provide insight into the biochemical composition of samples in a non-invasive manner. A primary challenge lies in extracting meaningful information from the large volumes of data generated through spectral imaging [17], [18]. Originally developed for remote sensing purposes [19], advancements in technology have enabled the proliferation of spectral imaging into diverse fields. These include precision agriculture [20], food quality evaluation [21], and medical applications [22], among others. Perfusion imaging represents one novel and promising application [23]. By noninvasively measuring physiological information, perfusion imaging may allow for the evaluation of organ function and disease monitoring.

The proposal in [24] employs multi-spectral imaging (MSI) and compares their results against tissue oxygen saturation (StO_2) from near-infrared reflectance spectroscopy (NIRS). The authors measure local tissue desaturation and reperfusion during two consecutive vascular occlusion tests. However, no detailed information exists on the methodology for estimating the MSI perfusion parameters. A total of 58 volunteers participated in this study, and the subject's systolic pressure was used as a control parameter. The authors induced a total occlusion by applying 30 mmHg above systolic pressure, and then the cuff was released until oxygen saturation was below 40%, according to NIRS measurements. Pearson's correlation was used to evaluate the level of agreement between the MSI and NIRS perfusion parameters. According to their results, the correlation was moderate (r = 0.42).

Other approaches are based on the combination of different systems, such is the case of [25]. In this study, the authors propose a laser speckle incorporated multispectral system to estimate StO_2 and a relative blood perfusion parameter. The multispectral channels in the green portion of the spectrum (530-570 nm) were utilized, and a model based on the Extended Beer Lambert Model was fitted using light attenuation. The authors assessed the application of this approach for monitoring the healing progression of skin grafting in patients with diabetic ulcers. Over a span of two years, approximately four sessions were conducted. The results were validated by comparing the outcomes between individuals with type II diabetes and foot ulcers, and a healthy control group. The participants were divided into two groups: one with positive healing and the other with impaired healing. However, the findings related to StO_2 revealed only a small mean absolute difference in comparison to the control group.

Hyper-spectral (HS) images is another technique that can measure reflectance data in the visible and near-infrared (VIS-NIR) range but with more wavelength bands available. These systems are also non-destructive, representing a great option for biomedical applications. Such is the case of in-vivo tumor boundary delimitation [26]. The authors built a database of HS images during neurosurgery procedures. They collected 36 HS images from 22 participants. The images were labeled by neurosurgeons to identify four classes of tissue: normal, primary, and secondary cancer, and a fourth class containing blood-vessels and background elements. In [27], the authors employ a commercially available system for clinical use that can record images with a spatial resolution of 640 × 480, and 100 spectral channels with a processing time of around 30 seconds. However, many of these approaches rely on prior information such as absorption and scattering coefficients [28]. In addition, they do not actually use all the available spectral information. The methods proposed in [29] can estimate perfusion parameters

in a clinical setting such as StO_2, hemoglobin, and water indexes. In this research line, the work in [30] established a key contribution, where the authors applied two different models and their inverses to obtain perfusion parameters. They used Markov-chain [31] and Kubelka-Munk models to estimate skin's parameters [32]. Hence, a hyper-spectral input image was used to estimate concentrations of melanin, blood volume, and blood-oxygen fractions along with the depth of the skin layers.

The main problem in estimating perfusion parameters through imaging methods is the lack of a proper validation. In-vivo validation is challenging due to ethical considerations, variability between populations and the sample size, as well as limited control of experimental conditions. Several diagnostic tests that, although they may be specific, are highly invasive, such as arterial blood gas analysis [33]. This exam requires a blood sample, from which oxygen levels, pH, and other information about tissue perfusion can be extracted. These tests are the gold standard for the calibration of oximetry devices [34]. To evaluate perfusion, another option is the application of occlusion tests to induce ischemia. These tests consist of the temporal restriction of blood flow to an area of interest. When applied to a limb, a simple tool such as a blood cuff, a tourniquet, or even a rubber band can be used for blood vessel blockage. When the pressure applied only restricts the blood flow in the veins, it is called venous occlusion. A total occlusion occurs when the blood circulation stops completely. When the blockage is released, the restoration of blood flow is called reperfusion. This condition can lead to hyperemia, which is a rapid and exaggerated reperfusion to the organs affected by ischemia [35]. The changes in oxygen levels might be useful to validate reperfusion parameters. However, perfusion parameters based on pulseoximetry might not register accurate readings during blood occlusion [36]. In contrast, it is possible to correctly measure these abrupt oxygen changes using NIRS or PPG readings [37].

Thus, our work introduces an open-source database for evaluating perfusion parameters in an upper limb. The database comprises sequences of multi-spectral images of the hand palm and PPG data from the thumb. The latter is used for validation purposes through the estimation of baseline perfusion parameters (changes in oxygenated and deoxygenated hemoglobin). The data is recorded in-vivo during the application of a occlusion protocol, inducing changes in the dominant hand palm for approximately 10 min. for each subject. In addition, we have conducted an initial evaluation of the data by using two well-known regression techniques: the Kubelka-Munk method and a linear model for monitoring skin perfusion parameters. These methods provide valuable insight into the data and can be used to validate perfusion MSI-based techniques.

The rest of the manuscript is organized as follows. A description of the experimental protocol and hardware, as well as the details of the processing algorithms and the validation stage, are provided in Section II. The characteristics of the database, and the results obtained to estimate hemoglobin changes during the induced hyperemia, are described in Section III. To conclude, the results are discussed, and the final remarks are presented in Section IV

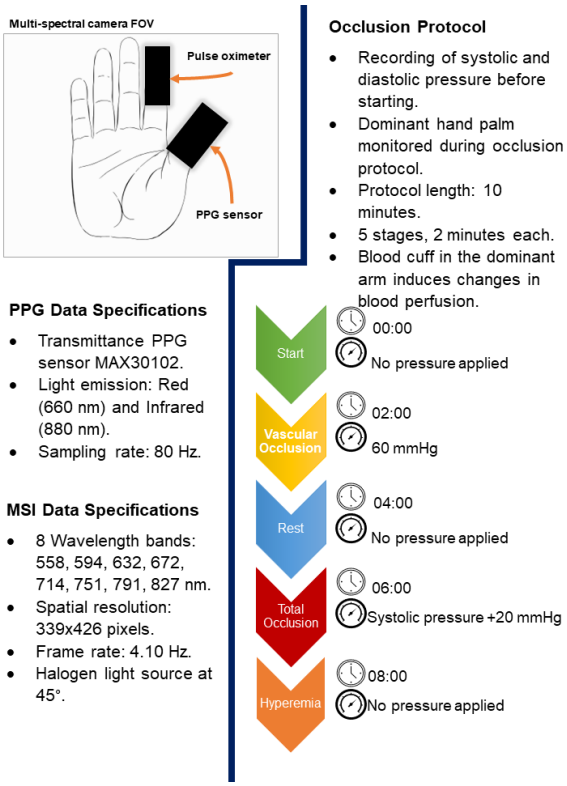

FIGURE 1. Summary of the methodology used to capture the database, highlighting key hardware components (MSI camera and PPG sensor). The field of view (FOV) and position of the sensors are depicted in the top image. The demographics of the study and an overview of the content of the database are listed in the left-bottom. In the right-bottom, a diagram of the five-stage occlusion protocol shows the acquisition sequence, including start time and applied pressure for each stage.

II. METHODOLOGY

In this section, we describe the experimental protocol used to generate the database, as well as the hardware employed for PPG and MSI data acquisition. We present the methodology to estimate different perfusion parameters with both acquisition approaches. Hence, the proposed methodology is summarized in Fig. 1.

A. EXPERIMENTAL PROTOCOL

This work aims to generate an open-source database to evaluate changes in tissue perfusion. To do so, we reproduced the protocol from [36], to induce key changes in blood oxygen levels. This protocol uses a blood pressure cuff to partially occlude the blood flow in an upper limb. This protocol is considered safe and was performed in line with the principles of the Declaration of Helsinki. We followed the guidelines of our institution for experiments involving human subjects and submitted the protocol to be reviewed by the Ethics Committee "*Comité Institucional de Bioética*" of the Universidad Autonoma de Aguascalientes in Mexico. The protocol was approved with the code: CIB-UAA-37.

Furthermore, the protocol was explained to each participant, and they were required to sign an informed consent to be included in this study. Participants were excluded according to the following criteria: any individual with a history of vascular disease or chronic conditions such as diabetes mellitus and hypertension was not eligible to participate. In addition, those with skin infections or abnormalities were also excluded to maintain the integrity of the study and to ensure an accurate assessment of tissue perfusion.

Before starting the protocol, the participants were given a minimum of 10 minutes to rest in a room set to ambient temperature. All testing was conducted between 9:00 and 15:00 hours, ensuring consistency. Each measurement stage was carried out in a unified laboratory setting, deliberately isolated from sunlight. The participants were seated and their superior limbs extended on a table. The blood pressure cuff, as well as all sensors, were placed in their dominant hand, which was recorded by the multi-spectral camera. A pulseoximeter was placed on the index finger while the PPG device on the thumb. These sensors and their cables were covered with black pasteboard to avoid reflections on the camera. First, the participant's systolic and diastolic pressures were sampled. Each experiment lasted 10 min. and the protocol was divided into five stages of two min. each one. During the first stage, data acquisition begins and no pressure is applied through the sphygmomanometer. The vascular occlusion (VO) stage starts at 2:00 min., where a fixed and constant 60 mmHg pressure is applied manually using the blood pressure cuff. At the beginning of the rest stage (4:00 min. mark), the pressure is released, and no pressure is applied. The total occlusion (TO) stage starts at 6:00 min., where pressure is constantly applied for the whole two min. This pressure is set to 20 mmHg above the registered systolic pressure for the participant. At the 8-min. mark, the pressure is released at the hyperemia stage, where the subject is allowed to rest. The experiment ends at ten min.

B. PHOTOPLETHYSMOGRAPHY DATA

Photoplethysmography data is used to obtain baseline perfusion parameters. For this goal, the PPG sensor MAX30102 is used [38]. This device is a transmittance PPG sensor that emits light using red (660 nm) and infrared (880 nm) LEDs. The light is sampled with a photodetector with a spectral range of sensitivity between 600 and 900 nm. The PPG sensor was controlled using an Arduino Mega microcontroller, through the I^2C interface. The sampling rate was fixed to 80 Hz. The components DC and AC were obtained according to the methodology in [39]. First, the supply voltage interference is filtered from both, red and infrared PPG channels. Then the signal peaks are localized to identify each cycle in the PPG measurements. The DC component is removed from the pulse baseline by a low-pass filter. Once the DC component is extracted from each PPG signal, the AC component is calculated as the difference between maximum and minimum values in a single PPG cycle. The components AC and DC of each PPG signal are the basis for estimating multiple perfusion parameters [40]. We estimated the ratio of absorbances defined as:

$$R_{PPG} = \frac{AC_{Red}/DC_{Red}}{AC_{IR}/DC_{IR}}, \tag{1}$$

where sub-index Red represents the PPG component recorded at 660 nm, and IR represents the measurement at 880 nm. There are several models in the literature to estimate peripheral capillary oxygen saturation (SpO_2), in this work we used the following definition from [39]:

$$SpO_2 = -45.06R_{PPG}^2 + 30.354R_{PPG} + 94.845. \tag{2}$$

The perfusion index measures the relationship between the AC and DC components [41]. In this work, we employed a definition based only on the IR measurement [40], according to the formula:

$$PI_{IR} = \frac{AC_{IR}}{DC_{IR}} \times 100. \tag{3}$$

Given the DC signal for each PPG channel, the light attenuation was calculated as:

$$\Delta A_{Red} = \ln\left(\frac{DC_{Red}(0)}{DC_{Red}}\right), \tag{4}$$

$$\Delta A_{IR} = \ln\left(\frac{DC_{IR}(0)}{DC_{IR}}\right), \tag{5}$$

where the index (0) represents the initial measurements during the protocol. In this work, we employed the average of the first 100 samples for each DC signal in every experiment. Next, we employ the solution proposed by [36] to estimate baseline perfusion parameters by the changes in oxygenated hemoglobin $\Delta[HbO_2]$ and deoxyhemoglobin $\Delta[Hb]$, which were calculated as:

$$\Delta[HbO_2] = \frac{\Delta A_{Red}\varepsilon_{IR}^{Hb} - \Delta A_{IR}\varepsilon_{Red}^{Hb}}{\varepsilon_{Red}^{HbO_2}\varepsilon_{IR}^{Hb} - \varepsilon_{IR}^{HbO_2}\varepsilon_{Red}^{Hb} \cdot d \cdot DPF}, \tag{6}$$

$$\Delta[Hb] = \frac{\Delta A_{IR}\varepsilon_{Red}^{HbO_2} - \Delta A_{Red}\varepsilon_{IR}^{HbO_2}}{\varepsilon_{Red}^{HbO_2}\varepsilon_{IR}^{Hb} - \varepsilon_{IR}^{HbO_2}\varepsilon_{Red}^{Hb} \cdot d \cdot DPF}, \tag{7}$$

where the molar extinction coefficients for each molecule and wavelength (ε_{Red}^{Hb}, $\varepsilon_{Red}^{HbO_2}$, ε_{IR}^{Hb}, $\varepsilon_{IR}^{HbO_2}$) were taken from [42]. As a result, these parameters were set to $\varepsilon_{Red}^{Hb} = 3.4408\ Mm^{-1}cm^{-1}$, $\varepsilon_{Red}^{HbO_2} = 0.3346\ Mm^{-1}cm^{-1}$, $\varepsilon_{IR}^{Hb} = 0.8412\ Mm^{-1}cm^{-1}$, and $\varepsilon_{IR}^{HbO_2} = 1.2846\,Mm^{-1}cm^{-1}$. Meanwhile, parameter d in (6) and (7) represents the distance between the light emitter and the detector, while DPF is the differential path factor. This data is not available for the MAX30102 sensor. Therefore, to estimate the changes proportional to [*absolute concentration*] × [*optical pathlenght*], we followed the methodology by Abay et al. [36], [37].

C. MULTI-SPECTRAL IMAGING DATA

In this work, we used a nine channels multi-spectral camera (SILIOS Technologies SA., France) model CMS-V1-C-EVR1M-USB3. The camera measures eight wavelength channels centered at

$$\Lambda = \{558, 594, 632, 672, 714, 751, 791, 827\} \quad \text{nm}. \tag{8}$$

The full-width half-maximum values for the camera channels are 26, 24, 25, 25, 27, 28, 31, 34 nm. The 9th channel records the average response from the other 8 channels. However, this information was not employed in our study. The scene was illuminated with a 150 W halogen light (Fiber-lite Mi-150 Illuminator Series, DolanJenner Industries, Boxborough, MA, USA). The camera was equipped with a polarizer (PS1000 VIS/SWIR Wire Grid Linear Polarizer Film), and the raw spatial resolution of each spectral image is 339 × 426 pixels. The camera was set to record multi-spectral images at a rate of 4.10 Hz with an exposure time of 16.70 ms.

At the processing stage, the images were cropped to 320 × 400. A mask was calculated to process pixel positions corresponding only to the subject's hand. To do so, we calculated the maximum value of the Euclidean norm of each image along the spectral dimension, and for every pixel with a value lower than 25%, this position was masked. Furthermore, pixels in the boundary regions of the limb were removed by applying morphological erosion with a disk kernel of ratio three. The set of all available pixels in the mask for a multi-spectral image is denoted as $\mathcal{P} \subset \mathbb{Z} \times \mathbb{Z}$.

A multi-spectral image at pixel position p and wavelength channel λ is denoted as $I(\mathrm{p}, \lambda)$, where $\mathrm{p} \in \mathcal{P}$ and $\lambda \in \Lambda$. The reflectance at channel λ and pixel p is obtained by a normalization step:

$$R(\mathrm{p}, \lambda) = \frac{I(\mathrm{p}, \lambda) - I_D(\mathrm{p}, \lambda)}{I_W(\mathrm{p}, \lambda) - I_D(\mathrm{p}, \lambda)} \quad \forall \mathrm{p} \in \mathcal{P},\ \lambda \in \Lambda \tag{9}$$

where $I_W(\mathrm{p}, \lambda)$ and $I_D(\mathrm{p}, \lambda)$ denote the corresponding white and dark reference images. In this work, we employed a polytetrafluoroethylene (PTFE) plate to generate the white reference $I_W(\mathrm{p}, \lambda)$ [43]. The dark reference $I_D(\mathrm{p}, \lambda)$ was captured by taking images with the lens cap on. Some methods to estimate perfusion parameters are based on the absorbance, which is defined as:

$$A(\mathrm{p}, \lambda) = -\ln\left(R\left(\mathrm{p}, \lambda\right)\right) \quad \forall \mathrm{p} \in \mathcal{P},\ \lambda \in \Lambda. \tag{10}$$

D. ESTIMATION OF MSI PERFUSION PARAMETERS

To demonstrate the value of the presented database, we evaluated two methods to estimate perfusion parameters based on regression techniques and multi-spectral images. These methods use reference spectral responses, i.e., tabulated spectral absorption coefficients measured in laboratory conditions or approximations [28], [44]. We analyzed a linear model based on absorbance [45], [46], [47], [48], and a non-linear model [30], [32], [49], [50] which is based on reflectance images. For this evaluation, we quantified perfusion parameters related to the contribution of hemoglobin in oxygenated HbO_2 and deoxygenated Hb forms using the MSI data. The results obtained were contrasted against the baseline PPG perfusion parameters.

The spectral absorption coefficients at λ wavelength channel were approximated [50] as:

$$\mu_{a.HbO_2}(\lambda) = \ln(10) \cdot e_{HbO_2}(\lambda) \cdot G/M[cm^{-1}] \quad \forall \lambda \in \Lambda, \tag{11}$$

$$\mu_{a.Hb}(\lambda) = \ln(10) \cdot e_{Hb}(\lambda) \cdot G/M[cm^{-1}] \tag{12}$$

where G represents the weight in grams per liter, and M is the gram molecular weight of hemoglobin. In these experiments, we set $G = 150$ g/l and $M = 64,500$ g/mol [50]. The values for the molar extinction coefficients e_{HbO_2} and e_{Hb} in $[cm - 1/(moles/liter)]$ were taken from [44] at the closest values tabulated for our wavelength channels in Λ.

The most common chromophore present in human skin is melanin, whose spectral absorption coefficient can be approximated by the next equation [32], [50]:

$$\mu_{a.mel}(\lambda) = 6.6 \times 10^{11} \lambda^{-3.33}[cm^{-1}] \quad \forall \lambda \in \Lambda. \tag{13}$$

1) LINEAR-MODEL

This model considers a minimal contribution of chromophores other than HbO_2 and Hb, and it has been used to evaluate oxygenation changes in hands occlusion [46], tumors [48] and validated in-vivo in an animal model [45]. According to this model, the estimated absorbance of incident light A_{LM} at channel λ is a linear combination of the chromophores:

$$A_{LM}(C_{HbO_2}, C_{Hb}, \alpha, \lambda) = C_{HbO_2} \cdot \mu_{a.HbO_2}(\lambda) + C_{Hb} \cdot \mu_{a.Hb}(\lambda) + \alpha \tag{14}$$

where $(C_{HbO_2}, C_{Hb}, \alpha)$ are scaling coefficients. In this work, we employed the absorption coefficients $\mu_{a.HbO_2}$ and $\mu_{a.Hb}$ from eqs. (11) and (12), respectively. This model concentrates the contribution from other chromophores in the bias term α. Given a subset of channels $\Lambda_A \subset \Lambda$, we estimate the optimal parameters $(C_{HbO_2}, C_{Hb}, \alpha)$ at each pixel $\mathrm{p} \in \mathcal{P}$ by minimizing the following cost function:

$$J_{LM} = \sum_{\lambda \in \Lambda_A} \left[A(\mathrm{p}, \lambda) - A_{LM}\left(C_{HbO_2}, C_{Hb}, \alpha, \lambda\right)\right]^2, \tag{15}$$

where $A(\mathrm{p}, \lambda)$ is the sampled absorbance from the multi-spectral camera in (10).

2) KUBELKA-MUNK MODEL

The Kubelka-Munk model was designed to describe light interactions in a multi-layer medium [51]. It is employed to estimate light reflectance based on the spectral absorption and scattering coefficients, and thickness of the materials. When applied to human skin, these layers correspond to the epidermis and dermis. The former contains melanin and other minor chromophores such as bilirubin, collagen, keratin, and carotene. However, melanin is the most abundant chromophore in the human skin, while the rest only present a minor contribution in healthy subjects. At wavelength channel λ, the optical absorption coefficient of the epidermis layer $\mu_{a.epi}(\lambda)$ is characterized as:

$$\mu_{a.epi}(\lambda) = f_{mel} \cdot \mu_{a.mel}(\lambda) + (1 - f_{mel})\mu_{a.baseline}(\lambda), \tag{16}$$

where f_{mel} is a free parameter. In (16), we employ the spectral absorption of melanin $\mu_{a.mel}(\lambda)$ defined in (13), and for the

baseline $\mu_{a.baseline}(\lambda)$, we employ the definition from [32] and [50]:

$$\mu_{a.baseline}(\lambda) = 0.244 + 85.3 \exp\left(\frac{-[\lambda - 164]}{66.2}\right) [cm^{-1}]. \tag{17}$$

Since the dermis contains blood vessels, this layer also presents hemoglobin-based chromophores. At wavelength channel λ, the dermis spectral absorption coefficient $\mu_{a.der}(\lambda)$ is defined as:

$$\begin{aligned}\mu_{a.der}(\lambda) = & f_{blood} \cdot (C_{oxy} \cdot \mu_{a.HbO_2}(\lambda)) \\ & + f_{blood} \cdot (1 - C_{oxy}) \cdot \mu_{a.Hb}(\lambda) \\ & + (1 - f_{blood}) \cdot \mu_{a.baseline}(\lambda)),\end{aligned} \tag{18}$$

where f_{blood} and C_{oxy} are free variables. In the case of the scattering coefficients of both layers, we employ the definition of [50], where they are considered the sum of the Mie and Rayleigh scattering coefficients at λ channel:

$$\mu_{s.Mie}(\lambda) = 2 \times 10^5 \times \lambda^{-1.5} \tag{19}$$

$$\mu_{s.Rayleigh}(\lambda) = 2 \times 10^{12} \times \lambda^{-4} \tag{20}$$

$$\begin{aligned}\mu_{s.epi}(\lambda) &= \mu_{s.der}(\lambda) \\ &= \mu_{s.Mie}(\lambda) + \mu_{s.Rayleigh}(\lambda).\end{aligned} \tag{21}$$

According to the Kubelka-Munk model, the absorbances from eqs. (16) and (18) and the scattering coefficients from (21) determine the amount of light moving in two opposite directions within the skin layers. The backward flux K and the forward flux variables β of each layer are defined as

$$K_{epi}(\lambda) = \sqrt{\mu_{a,epi}(\lambda)\left(\mu_{a,epi}(\lambda) + 2\mu_{s,epi}(\lambda)\right)} \tag{22}$$

$$K_{der}(\lambda) = \sqrt{\mu_{a,der}(\lambda)\left(\mu_{a,der}(\lambda) + 2\mu_{s,der}(\lambda)\right)} \tag{23}$$

$$\beta_{epi}(\lambda) = \sqrt{\frac{\mu_{a,epi}(\lambda)}{\mu_{a,epi}(\lambda) + 2\mu_{s,epi}(\lambda)}} \tag{24}$$

$$\beta_{der}(\lambda) = \sqrt{\frac{\mu_{a,der}(\lambda)}{\mu_{a,der}(\lambda) + 2\mu_{s,der}(\lambda)}}. \tag{25}$$

The reflectances R_{epi}, R_{der} and the light transmitted from the epidermis to the dermis T_{epi} have the following expressions (26)–(28), as shown at the bottom of the next page, where variables D_{der} and D_{epi} represent the thickness of each layer in the skin. The total reflectance [32], [50] measured at the surface of the skin R_{KM} is a function of the form

$$R_T(\lambda) = R_{epi}(\lambda) + \frac{T_{epi}(\lambda)^2 R_{der}(\lambda)}{1 - R_{epi}(\lambda) R_{der}(\lambda)}. \tag{29}$$

Given a fixed set of wavelengths $\Lambda_R \subset \Lambda$, the Kubelka-Munk models the light based on the absorption and scattering coefficients. Consequently, the total reflectance can be considered a function of the parameters given a set of frequencies

$$\begin{aligned}&R_{\mathrm{KM}}\left(f_{\mathrm{mel}}, f_{\mathrm{blood}}, C_{\mathrm{oxy}}, D_{\mathrm{dermis}}, D_{\mathrm{epi}}, \lambda\right) \\ &\quad = R_T(\lambda) \quad \forall \lambda \in \Lambda_R.\end{aligned} \tag{30}$$

The model parameters are estimated by fitting a reflectance sample (9) to the Kubelka-Muk reflectance model, such as equation (3) in [50]. The cost function used to identify the perfusion parameters is described next:

$$\begin{aligned}J_{KM} = \sum_{\lambda \in \Lambda_R} & \big[R(\mathrm{p}, \lambda) \\ & - R_{\mathrm{KM}}\left(f_{\mathrm{mel}}, f_{\mathrm{blood}}, C_{\mathrm{oxy}}, D_{\mathrm{dermis}}, D_{\mathrm{epi}}, \lambda\right)\big]^2\end{aligned} \tag{31}$$

where $R(\mathrm{p}, \lambda)$ is the sample reflectance from the multi-spectral camera in (9). Hence, the optimal parameters $\left(f_{\mathrm{mel}}, f_{\mathrm{blood}}, C_{\mathrm{oxy}}, D_{\mathrm{dermis}}, D_{\mathrm{epi}}\right)$ are obtained at each pixel $\mathrm{p} \in \mathcal{P}$ by minimizing the cost function in (31).

E. COMPARISON AND VALIDATION

The open-source database presented in this work consists of a video sequence of multi-spectral images and PPG data recorded in-vivo from multiple subjects. The PPG data serves as a reference for estimating perfusion parameters from the thumb. These values were compared against MSI perfusion parameters from the fingertip of the middle finger. We selected these locations based on the accuracy of the perfusion parameters measured in these positions, such as SpO_2 [52]. Due to the 10 min. duration of the occlusion protocol (see Fig. 1), maintaining a static posture for the subjects is challenging. Consequently, we implemented a tracking algorithm to monitor a region of interest (ROI) around the middle fingertip in the multi-spectral images and compare it with the thumb PPG data. This section elaborates on the ROI tracking and on the evaluation of the models for monitoring skin perfusion.

1) ROI AND TRACKING

In this study, we employed the Kanade-Lucas-Tomasi (KLT) feature tracking algorithm to track the fingertip movements of the participants [53]. We used the point tracker implementation from Matlab (Mathworks, Inc., Natick, Massachusetts, U.S.; v2020b). Initially, we manually selected a rectangular ROI surrounding the middle fingertip in the first frame for each participant video sequence. The features employed for tracking were corners detected using the features from the accelerated segment test (FAST) algorithm [54]. We conducted tracking on all participants every four frames throughout the entire experimental protocol. The ROI obtained from the tracking algorithm was multiplied with the energy mask (as described in Section II-C) to isolate and process only the middle fingertip region for estimating the MSI perfusion parameters.

2) EVALUATION OF REGRESSION METHODS

We estimated skin perfusion parameters by fitting the linear and Kubelka-Munk models to the input absorbance and reflectance signals, respectively. The perfusion parameters $(C_{HbO_2}, C_{Hb}, \alpha)$ in (14) were estimated using least squares regression. In a similar fashion to [45], we set all negative solutions to zero, as no constraints were applied. Meanwhile,

TABLE 1. Parameter ranges employed for the perfusion parameters estimated from the Kubelka-Munk model.

Parameter	Ranges
f_{mel}	0.0100-3.0100
f_{blood}	0.0010-0.5010
C_{oxy}	0.6000-0.9900
D_{epi}(cm)	0.0001-0.0006
D_{dermis}(cm)	0.0010-0.0040

to solve the regression problem in (31) for the perfusion parameters $\left(f_{\text{mel}}, f_{\text{blood}}, C_{\text{oxy}}, D_{\text{dermis}}, D_{\text{epi}}\right)$, we employed a particle swarm optimization method. We used the Matlab implementation provided with the optimization toolbox. The boundaries employed for each perfusion parameter in the Kubelka-Munk model are detailed in Table 1. The optimization method was configured to work with a swarm size of 50, 20 maximum simulations, and an error tolerance of 10^{-6}. All the signal processing was implemented in a Dell Precision 3660 workstation, equipped with a 12th generation Intel Core i7-12700K processor, and 16 GB of RAM. The preprocessing stages, as well as the implementations, were performed in Matlab.

In this way, there are three perfusion parameters that can be estimated from (15), and five from (31). However, we could not obtain reference values for melanin or other chromophores, nor the thickness of the skin layers. Therefore, we only perform a particular analysis of perfusion parameters related to hemoglobin, namely $(C_{HbO_2}, C_{Hb}, f_{\text{blood}}, C_{\text{oxy}})$. This study aims to evaluate if these parameters correlate with the measurements obtained by the PPG sensor.

In these identification processes of skin perfusion parameters, one important challenge is the selection of wavelength bands Λ_A and Λ_R. The regression methods in (15) and (31) are sensitive to prior information, since the spectral absorption and scattering coefficients are functions of the available wavelength bands Λ.

In this work, we perform an analysis to evaluate the Pearson correlation between MSI and PPG perfusion parameters during the application of the occlusion protocol. Our goal is to select the wavelength channels with better correlation against the PPG reference data, for both the linear model in (14) and the Kubelka-Munk in (30). The PPG reference values of $\Delta[HbO_2]$ in (6) and $\Delta[Hb]$ in (7) were interpolated to match the MSI framerate. Every four multi-spectral images, these values were correlated against $(C_{HbO_2}, C_{Hb}, f_{\text{blood}}, C_{\text{oxy}})$ using different wavelength configurations. We evaluated the perfusion parameters by employing different subsets in Λ. The linear model in (14) requires at least a couple of wavelength channels; however, feasible solutions were achieved using the following subsets:

$$\begin{aligned}
\Lambda_A^1 &= \{594, 632, 672\}\ \text{nm},\\
\Lambda_A^2 &= \{632, 791\}\ \text{nm},\\
\Lambda_A^3 &= \{632, 827\}\ \text{nm},\\
\Lambda_A^4 &= \{672, 791\}\ \text{nm},\\
\Lambda_A^5 &= \{672, 827\}\ \text{nm}.
\end{aligned} \tag{32}$$

In contrast, the Kubelka-Munk model in (30) predominantly exhibits accurate results for human skin when utilizing data in the visible range, so we used the following subsets:

$$\begin{aligned}
\Lambda_R^1 &= \{558, 594, 632, 672\}\ \text{nm},\\
\Lambda_R^2 &= \{558, 594, 632, 672, 714\}\ \text{nm},\\
\Lambda_R^3 &= \{558, 594, 632, 672, 714, 751\}\ \text{nm},\\
\Lambda_R^4 &= \{594, 632, 672, 714\}\ \text{nm},\\
\Lambda_R^5 &= \{594, 632, 672, 714, 751\}\ \text{nm}.
\end{aligned} \tag{33}$$

III. RESULTS

The open-source database presented in this work comprises records from 45 subjects who provided informed consent. The age of the participants ranged from 18 to 24 (mean = 20.17, SD = 1.73), with a majority being right-handed (44/45) and having Fitzpatrick Skin Type III (26 participants) and Type IV (19 participants). The information for each participant is summarized in Table 2.

Sequences of the multi-spectral images and PPG data from all recruited subjects are accessible in the following repository in Zenodo https://doi.org/10.5281/zenodo.7860900. The database contains at least 2,445 MSI for each participant, see Fig. 2. Each multi-spectral image consists of the nine single channels in PNG format, as detailed in subsection II-C. We opted for the PNG format due to its lossless compression and user-friendly metadata management, particularly for non-technical users like those in the medical field. This choice aligns with our goal of creating a database accessible to multidisciplinary research teams. Full hand and finger masks obtained from the tracking process are available. The raw

$$R_{epi}(\lambda) = \frac{\left(1-\beta_{epi}^2(\lambda)\right)\times\left(e^{K_{epi}(\lambda)D_{epi}(\lambda)} - e^{-K_{epi}(\lambda)D_{epi}(\lambda)}\right)}{\left(1+\beta_{epi}(\lambda)\right)^2 e^{K_{epi}D_{epi}} - \left(1-\beta_{epi}(\lambda)\right)^2 e^{-K_{epi}(\lambda)D_{epi}(\lambda)}} \tag{26}$$

$$R_{der}(\lambda) = \frac{\left(1-\beta_{der}^2(\lambda)\right)\times\left(e^{K_{der}(\lambda)D_{der}(\lambda)} - e^{-K_{der}(\lambda)D_{der}(\lambda)}\right)}{(1+\beta_{der}(\lambda))^2 e^{K_{der}(\lambda)D_{der}(\lambda)} - (1-\beta_{der}(\lambda))^2 e^{-K_{der}(\lambda)D_{der}(\lambda)}} \tag{27}$$

$$T_{epi}(\lambda) = \frac{4\beta_{epi}(\lambda)}{\left(1+\beta_{epi}(\lambda)\right)^2 e^{K_{epi}(\lambda)D_{epi}(\lambda)} - \left(1-\beta_{epi}(\lambda)\right)^2 e^{-K_{epi}(\lambda)D_{epi}(\lambda)}} \tag{28}$$

TABLE 2. Participants data in the experimental protocol, where the table presents information from each subject, identifiable by a unique code. Age, gender, and skin type (as per the Fitzpatrick scale) are reported. The systolic pressure recorded before the start stage of the protocol is also presented for each subject. In the following columns, the number of multi-spectral images per patient, each composed of nine channels, along with the length of data collection in minutes, seconds, and milliseconds are detailed. The last column indicates the occurrence of reactive hyperemia, marked by a decrease in $\Delta[HbO_2]$ and an increase in $\Delta[Hb]$ during the TO stage, as well as an inverse trend following the pressure release. The participants who presented high movement during the experiment are marked with a symbol *.

ID	Age	Gender	Skin type	Systolic P.	# Multi-spectral Images	Time Length	Hyperemia
P1	20	M	4	109	2,456	09:58:7960	yes
P2	20	M	3	129	2,458	09:59:2880	yes
P3	22	M	4	117	2,460	09:59:7730	yes
P4	19	F	3	110	2,454	09:58:3120	no
P5	18	F	4	106	2,458	09:59:2839	no
P6	18	F	4	111	2,471	10:02:4600	yes
P7	18	F	4	91	2,462	10:00:2630	yes
P8	18	F	4	102	2,474	10:03:1930	yes
P9	21	M	3	113	2,468	10:01:7300	yes
P10	19	F	3	108	2,461	10:00:0340	yes
P11	18	M	4	137	2,461	10:00:0210	yes
P12	18	F	3	132	2,457	09:59:0429	yes
P13	18	M	4	119	2,461	10:00:0210	yes
P14	18	F	4	100	2,460	09:59:7770	yes
P15	18	F	3	104	2,460	09:59:7740	yes
P16	18	M	3	126	2,462	10:00:2660	yes
P17*	18	F	3	105	2,469	10:01:9710	yes
P18	21	F	4	122	2,461	10:00:0200	no
P19	21	F	3	130	2,462	10:00:2660	yes
P20	21	F	3	106	2,457	09:59:0440	yes
P21	23	M	3	133	2,459	09:59:5290	yes
P22	23	M	3	134	2,471	10:02:4590	no
P23	21	F	3	115	2,472	10:02:6630	yes
P24	21	M	3	111	2,445	10:00:2220	yes
P25	21	M	3	116	2,460	09:59:7330	yes
P26	21	M	4	107	2,462	10:00:2310	yes
P27	21	F	4	106	2,460	09:59:7440	yes
P28	24	F	4	106	2,460	09:59:7720	yes
P29	22	M	4	125	2,460	09:59:7700	yes
P30	21	M	4	125	2,461	10:00:0150	yes
P31	21	F	3	100	2,472	10:02:6959	yes
P32	22	M	3	120	2,460	09:59:7720	yes
P33	21	M	4	127	2,461	10:00:0140	yes
P34	19	F	3	100	2,457	09:59:0400	yes
P35	19	F	3	108	2,460	09:59:7730	yes
P36	20	F	3	136	2,471	10:02:4570	yes
P37	19	M	4	129	2,457	09:59:0380	yes
P38*	19	M	3	128	2,463	10:00:5040	yes
P39*	18	M	3	111	2,479	10:04:4060	yes
P40	23	M	4	110	2,462	10:00:2570	yes
P41	21	M	3	130	2,465	10:00:9930	yes
P42	20	F	3	126	2,461	10:00:0170	yes
P43	22	F	3	125	2,459	09:59:5270	yes
P44	22	M	3	138	2,467	10:01:4820	yes
P45	22	M	4	104	2,461	10:00:0160	yes

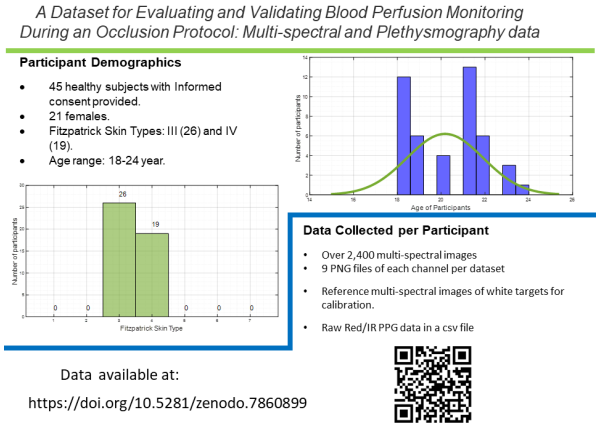

FIGURE 2. Infographic of the data available online upon request [55]. Raw data files for all the 45 participants, including PPG files and reference MSI data are available for the evaluation of novel perfusion parameters estimation methods.

PPG data is also included as simple comma-separated value files. Reference white material MSI data is also available to test different calibration methods.

Examples of multispectral images obtained for a single participant, at two different times (start and TO stages), during the occlusion protocol are displayed in Fig. 3. The perfusion parameters estimated at each location of the MSI can be arranged to obtain perfusion maps. These images provide spatially localized quantitative information that can assist physicians in diagnosing and monitoring tissue conditions without a biopsy. Examples of perfusion maps obtained for a single patient at different stages of the occlusion experiment are displayed in Fig. 4. While changes in C_{HbO_2}, C_{Hb}, and f_{mel} are evident, the magnitude of these changes is measured by evaluating the correlation between the values obtained from the middle finger and the reference PPG signals from the thumb.

For the initial evaluation of the database, the participants who presented excessive movement during the protocol (P17, P38, and P39) were excluded. Additionally, subjects who did not exhibit hyperemia during the occlusion protocol were also excluded (participants: P4, P5, P18, and P22). Consequently, the validation experiments presented in the subsequent subsections are based on data from 38 participants.

A. PPG PERFUSION PARAMETERS

The measurements obtained are shown in the Figs. 5 to 7. Figure 5 A) illustrates the range and mean values for the estimations of AC_{Red} and AC_{IR} by (4) and (5) in the thumb, respectively. The observed data aligns with measurements reported by Abay et al. [36], wherein a considerable decrease in AC values occurs during total occlusion (8:00 to 10:00 min). As depicted in Fig. 5 B), the DC components are also affected by the occlusion stages, with considerable inter-subject variability, particularly in the red component. Both DC_{Red} and DC_{IR} components exhibit a decline during the VO stage. However, during TO, DC_{Red} decreases, while DC_{IR} increases above nominal values.

The resulting ratio of absorbances R_{PPG} in (1) is presented in Fig. 5 C). This perfusion parameter displays high variability throughout the entire experiment, with multiple peaks occurring even in stages without blood cuff pressure. As observed during the protocol, the average value of R_{PPG} rises during occlusion stages at 2:00-4:00 min. (VO) and 6:00-8:00 min. (TO).

The SpO_2 range and mean values, as calculated from equation (2), are displayed in Fig. 6 A). This perfusion parameter also exhibits variability in the absence of applied pressure. It is worth noting that, according to the literature [56], values below 70% for SpO_2 are considered unreliable. This threshold is reached during occlusion stages, which is why this parameter is not included in the evaluation against MSI perfusion parameters. Next, Fig. 6 B) illustrates the estimation of PI_{IR} by (3). This perfusion parameter is sensitive to reperfusion occurring after each occlusion stage, particularly around 4:00 and 8:00 min. During total occlusion, the values of PI_{IR} drop considerably.

Figure 7 presents the changes in hemoglobin contribution $\Delta[HbO_2]$ and $\Delta[Hb]$ by (6) and (7), respectively. These values exhibit low inter-subject variability, particularly during the start (0:00-2:00 min.) and rest (4:00-6:00 min.) stages. The sampled signals are tolerant to occlusion protocols, as reported by Abay et al. [37]. Both range and mean signals decline during the VO stage and return to normal during the resting one. During TO (6:00-8:00 min.), the mean value of $\Delta[HbO_2]$ decreases, while $\Delta[Hb]$ increases. Upon the release of blood cuff pressure, the hyperemia stage (8:00-10:00 min.) is characterized by a rapid increase in $\Delta[HbO_2]$ levels and a decrease in $\Delta[Hb]$. Hence, the changes in these PPG perfusion parameters were utilized for the evaluation of MSI parameters.

B. MSI PERFUSION PARAMETERS CORRELATION

In this preliminary analysis, we sought to validate the effectiveness of MSI data for assessing the estimation of in-vivo perfusion parameters during an occlusion protocol. According to the literature [40], and the obtained PPG measurements (see Fig. 7, the parameters least prone to inconsistencies during an occlusion are $\Delta[HbO_2]$ and $\Delta[Hb]$. Nonetheless, the estimated signals for each parameter display a similar trend throughout the initial three stages of the protocol (start, VO and rest). In fact, during the VO stage (2:00-4:00 min.), both $\Delta[HbO_2]$ and $\Delta[Hb]$ tend to increase and subsequently revert to a baseline state during the rest stage (4:00-6:00 min). To avoid potential inaccuracies in the Pearson correlation-based evaluation, we focused on assessing the correlation outcomes for the signals $\Delta[HbO_2]$ and $\Delta[Hb]$ during the latter half of the experiment, starting from the 5:00 min. mark until the end.

1) CORRELATION BETWEEN $\Delta[HbO_2]$ AND MSI PERFUSION PARAMETERS

The $\Delta[HbO_2]$ reference measurements were obtained from the thumb of each participant, based on the PPG measurements (see Fig. 1). They were estimated by (6) and are shown

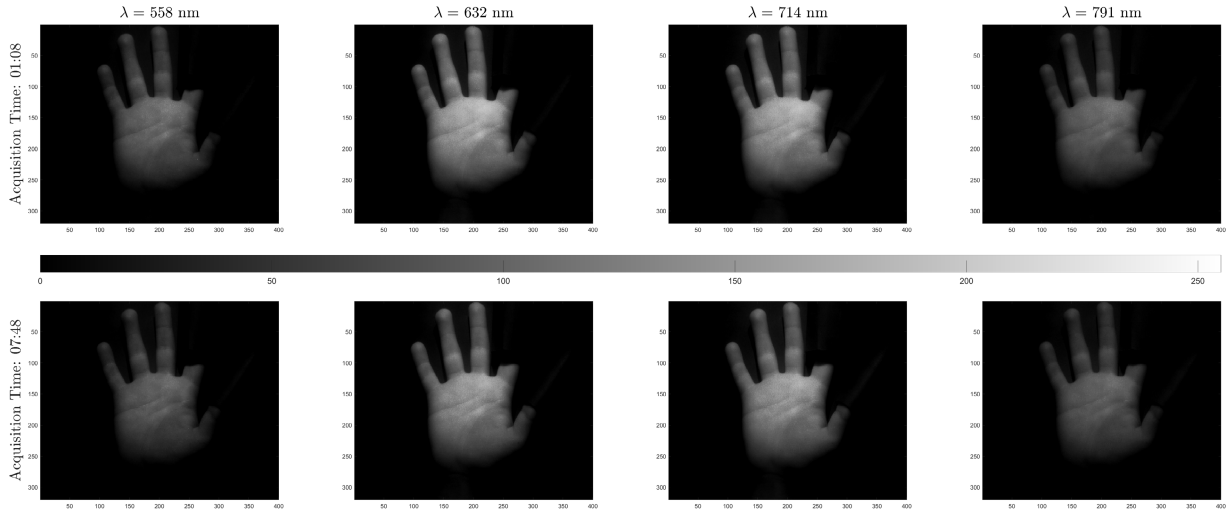

FIGURE 3. Four single channel images recorded for Participant #1. Each column displays the reflectance at 558, 632, 714 and 791 nm, respectively. The images on the bottom were recorded at 1 minute and 8 seconds from the start of the experiment (Start). Meanwhile, on the top, the images were recorded at 7 minutes and 48 seconds, near the end of the TO stage.

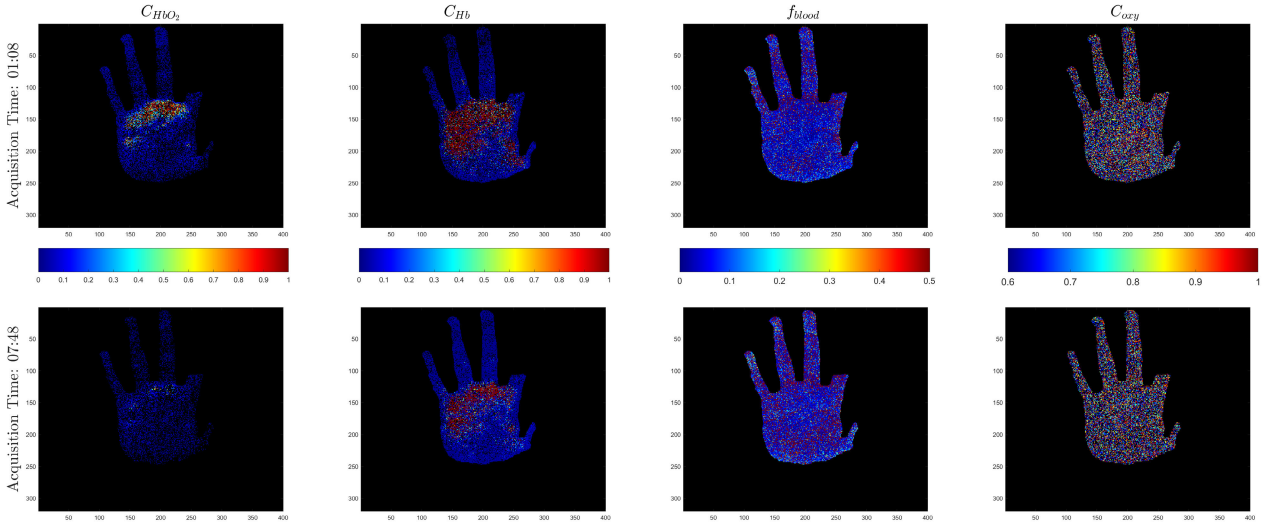

FIGURE 4. Perfusion Maps of 4 parameters related to hemoglobin and obtained during the Start (top row) and TO (bottom row) stages. The first and second columns depict the C_{HbO_2} and C_{Hb} maps estimated with the linear model. The third and fourth columns show the f_{blood} and C_{oxy} maps estimated with the Kubelka-Munk model, respectively.

in Fig. 7. We evaluated the Pearson correlation of this signal against the perfusion parameters (C_{HbO_2}, C_{Hb}, f_{blood} , C_{oxy}) from the linear and Kubelka-Munk models. These parameters were extracted from a ROI surrounding the middle fingertip, which was tracked throughout the occlusion protocol. The correlation calculated for the 38 participants, during the rest, TO, and hyperemia stages, employing the wavelength subsets in (32) and (33) are illustrated in violin plots in Figs. 8 to 11 [57].

First, the hemoglobin perfusion parameters (C_{HbO_2}, C_{Hb}) from the linear model in (14) exhibited mostly strong negative correlation values, with medians ranging from -0.5 to -0.7, as shown in Figs. 8 and 9. Nevertheless, a strong positive correlation was observed for C_{HbO_2} with a median of 0.8, using the subset Λ_A^2. This value represented the highest correlation with $\Delta[HbO_2]$ among all the MSI perfusion parameters evaluated. Next, we evaluated the blood perfusion parameters (f_{blood} , C_{oxy}) from the Kubelka-Munk model in (18). The estimated values of f_{blood} for different subsets Λ_R show weak negative correlations, see Fig. 10, with median values around -0.3. Meanwhile, according to the findings in Fig. 11, only three configurations yielded moderate to strong positive correlations with C_{oxy}.

2) CORRELATION BETWEEN $\Delta[Hb]$ AND MSI PERFUSION PARAMETERS

The correlation results for the PPG parameter $\Delta[Hb]$ in (7) and shown in Fig. 7, in relation to MSI perfu-

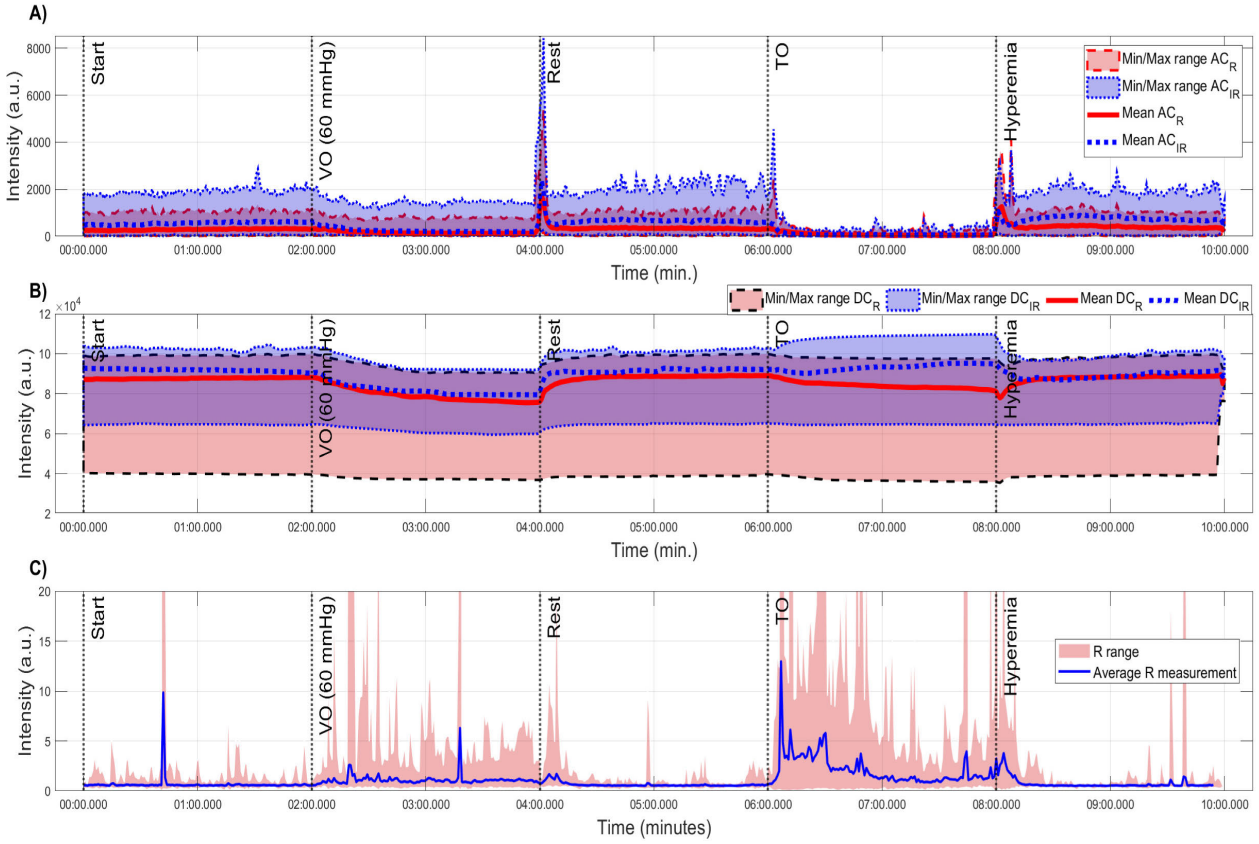

FIGURE 5. Range and average values of reference parameters measured using the PPG sensor throughout the occlusion protocol. Panel A) displays the AC_{Red} and AC_{IR} components, which are sensitive to the total occlusion applied at the beggining of the 8:00 minute mark. Panel B) shows the DC_{Red} and DC_{IR} signals, which do not register a considerable reduction during the occlusion stages. Panel C) shows R_{PPG} estimated by (1).

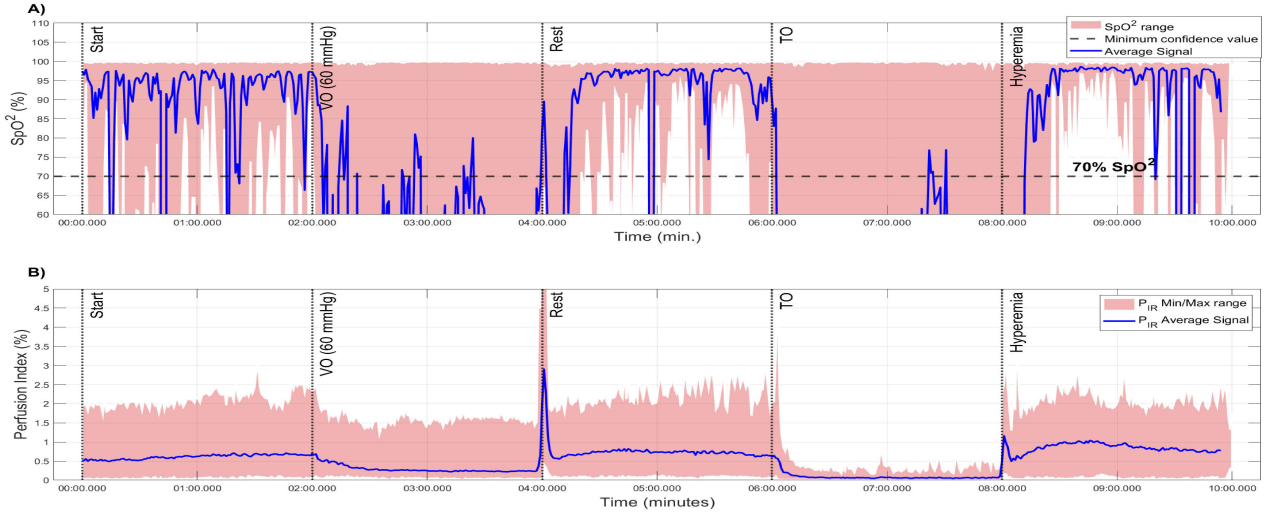

FIGURE 6. Panel A) displays the range and mean values of SpO_2 estimated using equation (2) throughout the occlusion experiment. SpO_2 values above the black dotted line are considered to be within an acceptable range. Panel B) shows PI_{IR} estimated using equation (3).

sion parameters, are presented in Figs. 12 to 15. The results for the linear model parameters (C_{HbO_2}, C_{Hb}) are illustrated in Figs. 12 and 13. A strong negative correlation between $\Delta[Hb]$ and C_{HbO_2} was anticipated; however, this trend was only observed for the subset λ_A^1, while the remaining configurations demonstrated strong positive correlations.

The correlation results with C_{Hb} were all highly positive, exhibiting median values around 0.8 for all wavelength subsets, which is consistent with expectations.

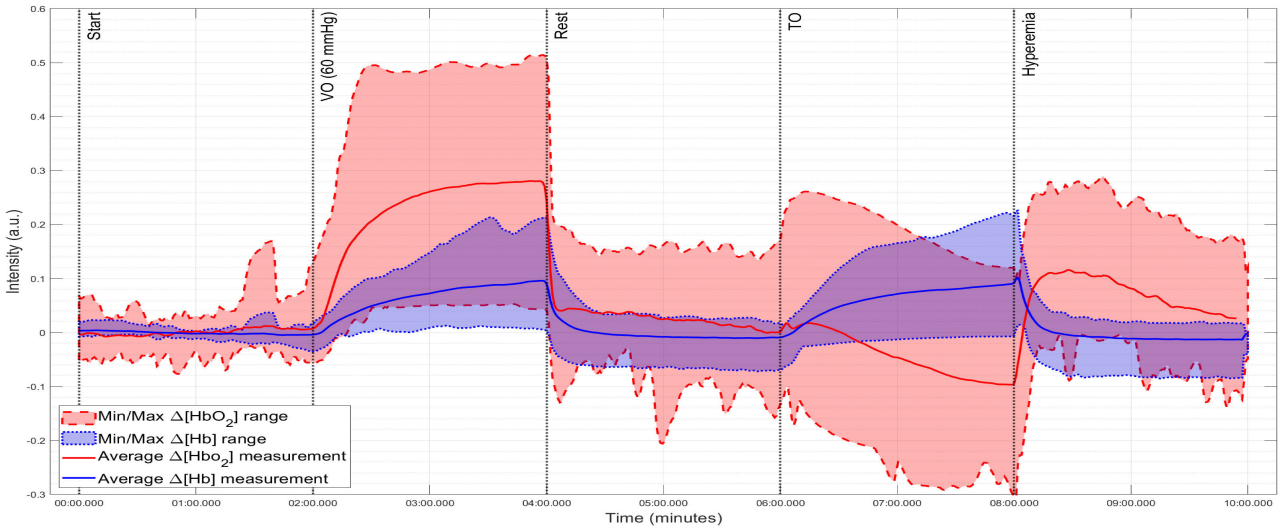

FIGURE 7. Range and mean values of $\Delta[HbO_2]$ and $\Delta[Hb]$ estimated by (6) and (7), respectively, for the 38 participants included in this analysis. These perfusion parameters are tolerant to total occlusion and illustrate the hyperemia and reperfusion phenomena around 08:00 min.

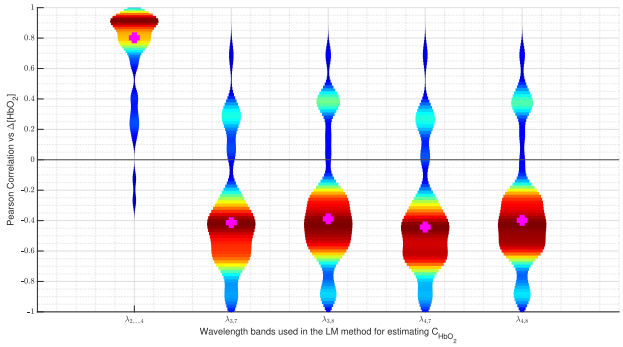

FIGURE 8. Distribution of the correlation results for $\Delta[HbO_2]$ vs C_{HbO_2} from the linear model 15. The median value is displayed with a magenta marker.

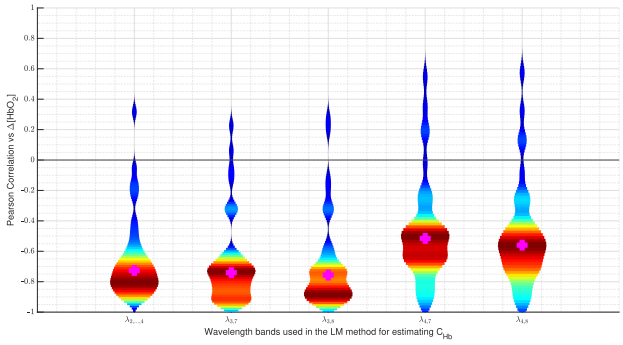

FIGURE 9. Distribution of the correlation results for $\Delta[HbO_2]$ vs C_{Hb} from the linear model 15. The median value is displayed with a magenta marker.

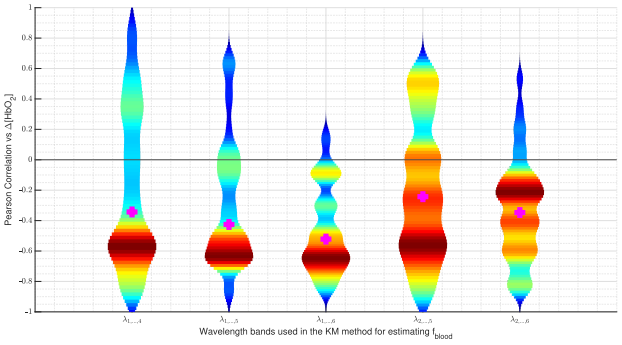

FIGURE 10. Distribution of the correlation results for $\Delta[HbO_2]$ vs f_{blood} from the Kubelka-Munk model 31. The median value is displayed with a magenta marker.

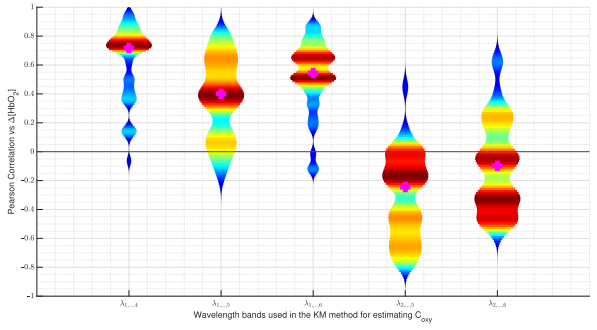

FIGURE 11. Distribution of the correlation results for $\Delta[HbO_2]$ vs C_{oxy} from the Kubelka-Munk model 31. The median value is displayed with a magenta marker.

On the other hand, the f_{blood} parameter from the Kubelka-Munk model demonstrated a strong positive correlation (0.72-0.82) across all wavelength subsets when compared with $\Delta[Hb]$, see Fig. 14. No clear trend emerged from the multiple implementations with C_{oxy} from the Kubelka-Munk model, see Fig. 15. However, these results are consistent with the results reported for $\Delta[HbO_2]$ in Fig. 11. This is, the results obtained for $\Delta[Hb]$ have an opposite sign to those obtained for $\Delta[HbO_2]$.

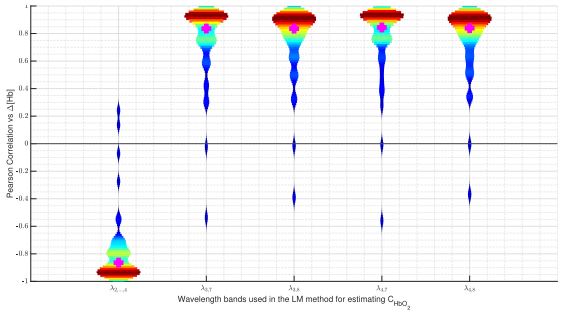

FIGURE 12. Distribution of the correlation results for $\Delta[Hb]$ vs C_{HbO_2} from the linear model 15. The median value is displayed with a magenta marker.

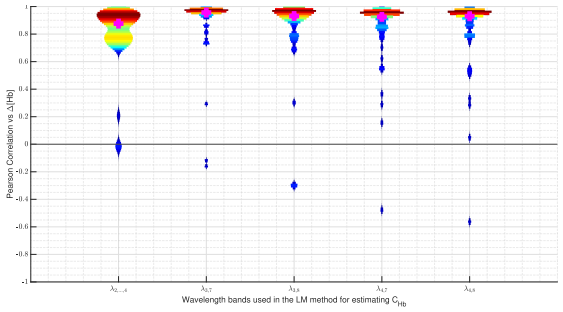

FIGURE 13. Distribution of the correlation results for $\Delta[Hb]$ vs C_{Hb} from linear model 15. The median value is displayed with a magenta marker.

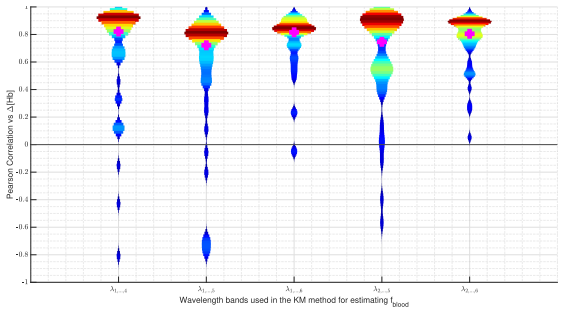

FIGURE 14. Distribution of the correlation results for $\Delta[Hb]$ vs f_{blood} from the Kubelka-Munk model 31 The median value is displayed with a magenta marker.

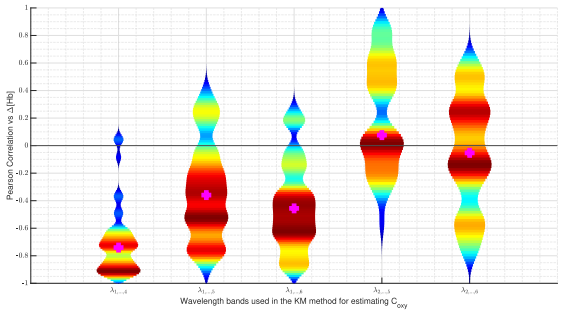

FIGURE 15. Distribution of the correlation results for $\Delta[Hb]$ vs C_{oxy} from the Kubelka-Munk model 31.The median value is displayed with a magenta marker.

IV. DISCUSSION

In this study, we developed an open-source database to measure changes in hemoglobin concentrations by a sequence of multi-spectral images. These changes were induced by a controlled occlusion protocol that lasts 10 min. During the protocol, MSI data from the hand palm and PPG measurements from the thumb were simultaneously recorded. The database comprises records from 45 test subjects who provided informed consent. The database can be accessed upon request via Zenodo [55]. We also conducted a preliminary evaluation of the database. Our analysis of the PPG measurements revealed certain parameter failures during the occlusion stages, particularly concerning SpO_2. The findings corroborate those of Abay et al. [36], demonstrating that $\Delta[HbO_2]$ and $\Delta[Hb]$, as estimated from PPG sensors, are sensitive to occlusion stages and capable of tracking phenomena such as reperfusion and hyperemia after blood cuff pressure release.

In an initial evaluation of the MSI data, we tested two regression approaches for estimating perfusion parameters. These methods are based on prior knowledge, particularly spectral absorption and scattering coefficients for the most prevalent chromophores in human skin. Our results confirmed strong correlations, both positive and negative, between PPG and MSI-based perfusion parameters. The preliminary outcomes indicate that MSI-based perfusion parameters can effectively measure changes in both oxygenated and deoxygenated hemoglobin. Additionally, the database provides valuable data for validation purposes, which is often challenging to obtain experimentally and is available for evaluating alternative MSI-based methodologies under a standardized protocol and controlled conditions. We anticipate that this database will be useful in validating novel methods based on MSI for in-vivo estimation of perfusion parameters. Finally, the study population is young and representative of the Mexican inhabitants, which exhibits minimal variation in skin phenotypes. However, the sample does not consider younger or older subjects. Owing to acquisition limitations, the evaluation was conducted using only a subset of the actual data. A total of 38 subjects with clean PPG data and observable hyperemia following the total occlusion stage were included in the analysis. Future research will be committed to the development of practical perfusion monitoring in clinical settings. Moreover, we aim to estimate perfusion parameters without prior information, such as assumptions about the sample population.

REFERENCES

[1] P. Shaw, A. K. Sharma, A. Kalonia, and S. K. Shukla, "Vascular perfusion: A predictive tool for thermal burn injury," *J. Tissue Viability*, vol. 29, no. 1, pp. 48–50, Feb. 2020.

[2] R. K. Rogers, M. Montero-Baker, M. Biswas, J. Morrison, and J. Braun, "Assessment of foot perfusion: Overview of modalities, review of evidence, and identification of evidence gaps," *Vascular Med.*, vol. 25, no. 3, pp. 235–245, Jun. 2020.

[3] Y. Monteerarat, R. Limthongthang, P. Laohaprasitiporn, and T. Vathana, "Reliability of capillary refill time for evaluation of tissue perfusion in simulated vascular occluded limbs," *Eur. J. Trauma Emergency Surg.*, vol. 2022, pp. 1–7, Jan. 2022.

[4] B. Ruaro, M. G. Nallino, A. Casabella, F. Salton, P. Confalonieri, A. De Tanti, and C. Bruni, "Monitoring the microcirculation in the diagnosis and follow-up of systemic sclerosis patients: Focus on pulmonary and peripheral vascular manifestations," *Microcirculation*, vol. 27, no. 8, pp. 1–12, Nov. 2020.

[5] R. Kumar, R. J. Gush, C. E. Murdoch, and N. Krstajić, "Simultaneous white light and laser speckle contrast imaging for in-vivo blood flow imaging during laparoscopic surgery: An alternative to fluorescence-based endoscopy," *Proc. SPIE*, vol. 11937, Mar. 2022, Art. no. 1193702.
[6] R. Aughwane, N. Mufti, D. Flouri, K. Maksym, R. Spencer, M. Sokolska, G. Kendall, D. Atkinson, A. Bainbridge, J. Deprest, T. Vercauteren, S. Ourselin, A. David, and A. Melbourne, "Magnetic resonance imaging measurement of placental perfusion and oxygen saturation in early-onset fetal growth restriction," *BJOG, Int. J. Obstetrics Gynaecol.*, vol. 128, no. 2, pp. 337–345, Jan. 2021.
[7] C. Huang, J. Liang, X. Lei, X. Xu, Z. Xiao, and L. Luo, "Diagnostic performance of perfusion computed tomography for differentiating lung cancer from benign lesions: A meta-analysis," *Med. Sci. Monitor*, vol. 25, pp. 3485–3494, May 2019.
[8] G. Dinsdale, S. Wilkinson, J. Wilkinson, T. L. Moore, J. B. Manning, M. Berks, E. Marjanovic, M. Dickinson, A. L. Herrick, and A. K. Murray, "State-of-the-art technologies provide new insights linking skin and blood vessel abnormalities in SSc-related disorders," *Microvascular Res.*, vol. 130, Jul. 2020, Art. no. 104006.
[9] A. Karlas, M. Kallmayer, N. Fasoula, E. Liapis, M. Bariotakis, M. Krönke, M. Anastasopoulou, J. Reber, H. Eckstein, and V. Ntziachristos, "Multispectral optoacoustic tomography of muscle perfusion and oxygenation under arterial and venous occlusion: A human pilot study," *J. Biophotonics*, vol. 13, no. 6, pp. 1–6, Jun. 2020.
[10] W. Li, J. Xia, G. Zhang, H. Ma, B. Liu, L. Yang, Y. Zhou, X. Dong, F. Fu, and X. Shi, "Fast high-precision electrical impedance tomography system for real-time perfusion imaging," *IEEE Access*, vol. 7, pp. 61570–61580, 2019.
[11] W. Huber, R. Zanner, G. Schneider, R. Schmid, and T. Lahmer, "Assessment of regional perfusion and organ function: Less and non-invasive techniques," *Frontiers Med.*, vol. 6, p. 50, Mar. 2019.
[12] I. N. de Keijzer, D. Massari, M. Sahinovic, M. Flick, J. J. Vos, and T. W. L. Scheeren, "What is new in microcirculation and tissue oxygenation monitoring?" *J. Clin. Monitor. Comput.*, vol. 36, no. 2, pp. 291–299, Apr. 2022.
[13] M. Kumar, J. W. Suliburk, A. Veeraraghavan, and A. Sabharwal, "PulseCam: A camera-based, motion-robust and highly sensitive blood perfusion imaging modality," *Sci. Rep.*, vol. 10, no. 1, pp. 1–17, Mar. 2020.
[14] V. Gupta and V. K. Sharma, "Skin typing: Fitzpatrick grading and others," *Clinics Dermatol.*, vol. 37, no. 5, pp. 430–436, Sep. 2019.
[15] S. Rahman, A. Iskandarova, M. E. Horowitz, K. K. Sanghavi, K. T. Aziz, N. Durr, and A. M. Giladi, "Assessing hand perfusion with Eulerian video magnification and waveform extraction," *J. Hand Surg.*, vol. 2022, pp. 1–22, Aug. 2022.
[16] Y. Garini, I. T. Young, and G. McNamara, "Spectral imaging: Principles and applications," *Cytometry A*, vol. 69A, no. 8, pp. 735–747, 2006.
[17] M. Wang, D. Hong, Z. Han, J. Li, J. Yao, L. Gao, B. Zhang, and J. Chanussot, "Tensor decompositions for hyperspectral data processing in remote sensing: A comprehensive review," *IEEE Geosci. Remote Sens. Mag.*, vol. 11, no. 1, pp. 26–72, Mar. 2023.
[18] Y. Xu, Q. Du, and N. Younan, "Particle swarm optimization-based band selection for hyperspectral target detection," in *Proc. IEEE Int. Geosci. Remote Sens. Symp. (IGARSS)*, Jul. 2016, pp. 5872–5875.
[19] P. Wang, L. Wang, H. Leung, and G. Zhang, "Super-resolution mapping based on spatial–spectral correlation for spectral imagery," *IEEE Trans. Geosci. Remote Sens.*, vol. 59, no. 3, pp. 2256–2268, Mar. 2021.
[20] A. Mancini, E. Frontoni, and P. Zingaretti, "Satellite and UAV data for precision agriculture applications," in *Proc. Int. Conf. Unmanned Aircr. Syst. (ICUAS)*, Jun. 2019, pp. 491–497.
[21] X. Xia, W. Liu, L. Wang, and J. Sun, "HSIFoodIngr-64: A dataset for hyperspectral food-related studies and a benchmark method on food ingredient retrieval," *IEEE Access*, vol. 11, pp. 13152–13162, 2023.
[22] N. T. Clancy, G. Jones, L. Maier-Hein, D. S. Elson, and D. Stoyanov, "Surgical spectral imaging," *Med. Image Anal.*, vol. 63, Jul. 2020, Art. no. 101699.
[23] A. Schmidt, F. Nießner, T. von Woedtke, and S. Bekeschus, "Hyperspectral imaging of wounds reveals augmented tissue oxygenation following cold physical plasma treatment in vivo," *IEEE Trans. Radiat. Plasma Med. Sci.*, vol. 5, no. 3, pp. 412–419, May 2021.
[24] A. A. Bruins, D. G. P. J. Geboers, J. R. Bauer, J. H. G. M. Klaessens, R. M. Verdaasdonk, and C. Boer, "The vascular occlusion test using multispectral imaging: A validation study," *J. Clin. Monitor. Comput.*, vol. 35, no. 1, pp. 113–121, Feb. 2021.
[25] S. P. Philimon and A. K. C. Huong, "Laser speckle integrated multispectral imaging system for in-vivo assessment of diabetic foot ulcer healing: A clinical study," *IEEE Access*, vol. 9, pp. 23726–23736, 2021.
[26] H. Fabelo et al., "In-vivo hyperspectral human brain image database for brain cancer detection," *IEEE Access*, vol. 7, pp. 39098–39116, 2019.
[27] M. Dietrich, S. Marx, M. von der Forst, T. Bruckner, F. C. F. Schmitt, M. O. Fiedler, F. Nickel, A. Studier-Fischer, B. P. Müller-Stich, T. Hackert, T. Brenner, M. A. Weigand, F. Uhle, and K. Schmidt, "Bedside hyperspectral imaging indicates a microcirculatory sepsis pattern—An observational study," *Microvascular Res.*, vol. 136, Jul. 2021, Art. no. 104164.
[28] S. L. Jacques, "Optical properties of biological tissues: A review," *Phys. Med. Biol.*, vol. 58, no. 11, pp. R37–R61, Jun. 2013.
[29] A. Holmer, J. Marotz, P. Wahl, M. Dau, and P. W. Kämmerer, "Hyperspectral imaging in perfusion and wound diagnostics—Methods and algorithms for the determination of tissue parameters," *Biomed. Eng.*, vol. 63, no. 5, pp. 547–556, Oct. 2018.
[30] L. Annala and I. Pölönen, "Kubelka–Munk model and stochastic model comparison in skin physical parameter retrieval," in *Computational Sciences and Artificial Intelligence in Industry* (Intelligent Systems, Control and Automation: Science and Engineering), vol. 76, T. Tuovinen, J. Periaux, and P. Neittaanmäki, Eds. Cham, Switzerland: Springer, 2022, doi: 10.1007/978-3-030-70787-3_10.
[31] L. Annala, S. Äyrämö, and I. Pölönen, "Comparison of machine learning methods in stochastic skin optical model inversion," *Appl. Sci.*, vol. 10, no. 20, p. 7097, Oct. 2020.
[32] R. Jolivot, Y. Benezeth, and F. Marzani, "Skin parameter map retrieval from a dedicated multispectral imaging system applied to dermatology/cosmetology," *J. Biomed. Imag.*, vol. 2013, p. 26, Jan. 2013.
[33] J. B. West, D. L. Wang, G. K. Prisk, J. M. Fine, A. Bellinghausen, M. Light, and D. R. Crouch, "Noninvasive measurement of pulmonary gas exchange: Comparison with data from arterial blood gases," *Amer. J. Physiol.-Lung Cellular Mol. Physiol.*, vol. 316, no. 1, pp. L114–L118, Jan. 2019.
[34] I. Badiola, V. Blazek, V. J. Kumar, B. George, S. Leonhardt, and C. H. Antink, "Accuracy enhancement in reflective pulse oximetry by considering wavelength-dependent pathlengths," *Physiolog. Meas.*, vol. 43, no. 9, Sep. 2022, Art. no. 095001.
[35] G. Bade, D. S. Chandran, A. Kumar Jaryal, A. Talwar, and K. K. Deepak, "Contribution of systemic vascular reactivity to variability in pulse volume amplitude response during reactive hyperemia," *Eur. J. Appl. Physiol.*, vol. 119, no. 3, pp. 753–760, Mar. 2019.
[36] T. Y. Abay and P. A. Kyriacou, "Reflectance photoplethysmography as noninvasive monitoring of tissue blood perfusion," *IEEE Trans. Biomed. Eng.*, vol. 62, no. 9, pp. 2187–2195, Sep. 2015.
[37] T. Y. Abay and P. A. Kyriacou, "Photoplethysmography for blood volumes and oxygenation changes during intermittent vascular occlusions," *J. Clin. Monitor. Comput.*, vol. 32, no. 3, pp. 447–455, Jun. 2018.
[38] *Max30102 High-Sensitivity Pulse Oximeter and Heart-Rate Sensor for Wearable Health*, Maxim Integrated, San Jose, CA, USA, Jan. 2018.
[39] S. K. Longmore, G. Y. Lui, G. Naik, P. P. Breen, B. Jalaludin, and G. D. Gargiulo, "A comparison of reflective photoplethysmography for detection of heart rate, blood oxygen saturation, and respiration rate at various anatomical locations," *Sensors*, vol. 19, no. 8, p. 1874, Apr. 2019.
[40] T. Y. Abay and P. A. Kyriacou, "Comparison of NIRS, laser Doppler flowmetry, photoplethysmography, and pulse oximetry during vascular occlusion challenges," *Physiolog. Meas.*, vol. 37, no. 4, pp. 503–514, Apr. 2016.
[41] M. Coutrot, E. Dudoignon, J. Joachim, E. Gayat, F. Vallée, and F. Dépret, "Perfusion index: Physical principles, physiological meanings and clinical implications in anaesthesia and critical care," *Anaesthesia Crit. Care Pain Med.*, vol. 40, no. 6, Dec. 2021, Art. no. 100964.
[42] M. Cope, *The Development of a Near Infrared Spectroscopy System and Its Application for non Invasive Monitoring of Cerebral Blood and Tissue Oxygenation in the Newborn Infants*. London, U.K.: University of London, 1991.
[43] M. S. Shaikh, K. Jaferzadeh, B. Thörnberg, and J. Casselgren, "Calibration of a hyper-spectral imaging system using a low-cost reference," *Sensors*, vol. 21, no. 11, p. 3738, May 2021.
[44] S. Prahl. (1999). *Optical Absorption of Hemoglobin*. [Online]. Available: https://omlc.org/spectra/hemoglobin/
[45] N. T. Clancy, S. Arya, D. Stoyanov, M. Singh, G. B. Hanna, and D. S. Elson, "Intraoperative measurement of bowel oxygen saturation using a multispectral imaging laparoscope," *Biomed. Opt. Exp.*, vol. 6, no. 10, pp. 4179–4190, 2015.

[46] K. J. Zuzak, M. D. Schaeberle, E. N. Lewis, and I. W. Levin, "Visible reflectance hyperspectral imaging: Characterization of a noninvasive, in vivo system for determining tissue perfusion," *Anal. Chem.*, vol. 74, no. 9, pp. 2021–2028, May 2002.
[47] S. P. Nighswander-Rempel, R. A. Shaw, V. V. Kupriyanov, J. Rendell, B. Xiang, and H. H. Mantsch, "Mapping tissue oxygenation in the beating heart with near-infrared spectroscopic imaging," *Vibrational Spectrosc.*, vol. 32, no. 1, pp. 85–94, Aug. 2003.
[48] B. S. Sorg, B. J. Moeller, O. Donovan, Y. Cao, and M. W. Dewhirst, "Hyperspectral imaging of hemoglobin saturation in tumor microvasculature and tumor hypoxia development," *J. Biomed. Opt.*, vol. 10, no. 4, 2005, Art. no. 044004.
[49] L. Gevaux, C. Adnet, P. Séroul, R. Clerc, A. Trémeau, J. L. Perrot, and M. Hébert, "Three-dimensional maps of human skin properties on full face with shadows using 3-D hyperspectral imaging," *J. Biomed. Opt.*, vol. 24, no. 6, 2019, Art. no. 066002.
[50] C. Li, V. Brost, Y. Benezeth, F. Marzani, and F. Yang, "Design and evaluation of a parallel and optimized light–tissue interaction-based method for fast skin lesion assessment," *J. Real-Time Image Process.*, vol. 15, no. 2, pp. 407–420, Aug. 2018.
[51] R. R. Anderson and J. A. Parrish, "The optics of human skin," *J. Investigative Dermatol.*, vol. 77, no. 1, pp. 13–19, Jul. 1981.
[52] G. Basaranoglu, M. Bakan, T. Umutoglu, S. U. Zengin, K. Idin, and Z. Salihoglu, "Comparison of SpO_2 values from different fingers of the hands," *SpringerPlus*, vol. 4, no. 1, p. 561, Dec. 2015.
[53] B. D. Lucas and T. Kanade, "An iterative image registration technique with an application to stereo vision," in *Proc. 7th Int. J. Conf. Artif. Intell.*, vol. 2, Aug. 1981, pp. 674–679.
[54] E. Rosten and T. Drummond, "Fusing points and lines for high performance tracking," in *Proc. 10th IEEE Int. Conf. Comput. Vis. (ICCV)*, 2005, pp. 1508–1515.
[55] O. Gutierrez-Navarro, L. Granados-Castro, A. R. Mejia-Rodriguez, and D. U. Campos-Delgado, "A dataset for evaluating and validating blood perfusion monitoring during an occlusion protocol: Multi-spectral and plethysmography data (1.0)," Zenodo, 2023, doi: 10.5281/zenodo.8157100.
[56] E. D. Chan, M. M. Chan, and M. M. Chan, "Pulse oximetry: Understanding its basic principles facilitates appreciation of its limitations," *Respiratory Med.*, vol. 107, no. 6, pp. 789–799, Jun. 2013.
[57] Jonas. (2023). Violin Plots for Plotting Multiple Distributions (distributionPlot.m). MATLAB Central File Exchange. Accessed: Mar. 15, 2023. [Online]. Available: https://www.mathworks.com/matlabcentral/fileexchange/23661-violin-plots-for-plotting-multiple-distributions-distributionplot-m

OMAR GUTIERREZ-NAVARRO (Member, IEEE) received the Bachelor of Science degree in electronics engineering from Universidad Autónoma of San Luis Potosí (UASLP), Mexico, in 2007, the Master of Science degree in computer science and industrial mathematics from Centro de Investigacion en Matematicas (CIMAT), Guanajuato, Mexico, in 2010, and the Ph.D. degree in electronics engineering from UASLP, in 2015, concentrating on numerical methods for characterizing in-vivo tissue through time-resolved fluorescence lifetime imaging microscopy data. In 2012, he was awarded with the Fulbright-Garcia Robles Grant, facilitating his research as a Visiting Scholar with the Biomedical Engineering Department, Texas A&M University. He joined the Biomedical Engineering Department, Universidad Autonoma de Aguascalientes, in 2015. His research interests include signal processing, machine learning, and multi/hyperspectral imaging applications within food science and biomedical engineering.

LILIANA GRANADOS-CASTRO received the B.Sc. degree in biomedical engineering and the M.Sc. degree in computer science and artificial intelligence from Universidad Autónoma de Aguascalientes, Aguascalientes, Mexico, in 2017 and 2020, respectively. She is currently pursuing the Ph.D. degree in biomedical engineering with Universidad Autonoma de San Luis Potosi, San Luis Potosi, Mexico. She made a research stay from Universidad Tecnológica de Panama, in 2019, and Universidad de Las Palmas de Gran Canaria, in 2022. Her research interests include photoplethysmography, pulse-oximetry, spectral imaging, and blood perfusion on large body areas.

ALDO RODRIGO MEJIA-RODRIGUEZ received the B.S. and Master of Science degrees in biomedical engineering from UAM-I, Mexico City, Mexico, in 2006 and 2009, respectively, and the Ph.D. degree in bioengineering from Politecnico di Milano, Milan, Italy, in 2013. Since June 2014, he has been a Faculty Member of biomedical engineering and the Postgraduates Programs on Electronic Engineering and Life Sciences with the School of Sciences, Universidad Autónoma de San Luis Potosi (UASLP). His research work focuses mainly on the processing and analysis of medical images for clinical applications, and the design and analysis of biomedical instrumentation for wearable devices and support systems in clinical decision making. He was involved in the organization of conferences related to biomedical engineering, such as ENIBET 2018 and 2019 (Conference Chair), CLAIB 2019 (Scientific Challenge Chair), CNIB 2020 (Conference Chair), EMBC-IEEE 2021 (Theme Chair–Biomedical Imaging and Image Processing), and CNBI 2023 (Theme Chair–AI, Modeling and Simulation of Biological Systems, Bioinformatics and Computational Biology). He was an Associate Editor of the *Mexican Journal of Biomedical Engineering* (*Revista Mexicana de Ingeniería Biomédica*—RMIB), from January 2020 to December 2021.

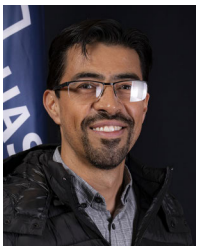

DANIEL U. CAMPOS-DELGADO (Senior Member, IEEE) received the B.S. degree in electronics engineering from Universidad Autónoma of San Luis Potos (UASLP), Mexico, in 1996, and the M.S.E.E. and Ph.D. degrees in electrical engineering from Louisiana State University (LSU), USA, in 1999 and 2001, respectively. In 2001, he joined the School of Science, UASLP, as a Professor. From July 2016 to June 2020, he was the Head of the School of Science. Since January 2021, he was appointed as the Director of the Institute for Optical Communication Research, UASLP. He has been an advisor or a co-advisor of 27 bachelor's thesis projects, 22 master's thesis works, and eight Ph.D. dissertations. His research interests include estimation and detection, optimization algorithms, fault diagnosis, artificial intelligence, and signal processing. He is currently a member of the Mexican Academy of Sciences (AMC). In 2001, the College of Engineering, LSU, granted him the Exemplary Dissertation Award. In 2009 and 2013, he received awards as a Young Researcher from UASLP and AMC. From May 2019 to September 2022, he was an Associate Editor of *IEEE Latin America Transactions* (ISSN: 1548-0992). Since October 2022, he has been the Deputy Editor-in-Chief of *IEEE Latin America Transactions*.